Journal of Alloys and Compounds 695 (2017) 1900–1907

Contents lists available at ScienceDirect

Journal of Alloys and Compounds

journal homepage: http://www.elsevier.com/locate/jalcom

Synthesis and properties of indium-doped hematite

Stjepko Krehula [a, *], Mira Ristić [a], Michael Reissner [b], Shiro Kubuki [c], Svetozar Musić [a]

[a] Division of Materials Chemistry, Ruđer Bošković Institute, P.O. Box 180, HR-10002, Zagreb, Croatia
[b] Institute of Solid State Physics, TU Wien, A-1040, Wien, Austria
[c] Department of Chemistry, Graduate School of Science and Engineering, Tokyo Metropolitan University, Minami-Osawa 1-1, Hachi-Oji, Tokyo, 192-0397, Japan

ARTICLE INFO

Article history:
Received 15 September 2016
Received in revised form
31 October 2016
Accepted 2 November 2016
Available online 3 November 2016

Keywords:
Hematite
Indium
Mössbauer spectroscopy
Morin transition
X-ray diffraction
FE-SEM

ABSTRACT

Indium-doped hematite samples were prepared by calcination of indium-doped goethite samples and investigated using different instrumental techniques. In^{3+}-for-Fe^{3+} substitution in the hematite structure was confirmed by the determination of the unit cell expansion using X-ray powder diffraction and by the measurement of the hyperfine magnetic field reduction using Mössbauer spectroscopy. Indium substitution in hematite also caused a decrease in the crystallite size, an increase in the particle size, a shift in the position of bands in infrared spectra, a decrease in the relative intensity of absorption bands in UV–Vis–NIR spectra and a disappearance of the Morin transition. Maximum substitution was estimated at about 8 mol%.

1. Introduction

Hematite (α-Fe_2O_3), often present in rocks and soils, is the most stable iron oxide under ambient conditions [1,2]. It crystallizes in the trigonal crystal system, space group $R\bar{3}c$, hexagonal unit cell parameters $a = 5.038$ Å, $c = 13.772$ Å [3]. Hematite crystal structure is based on the hexagonal close packing of O^{2-} ions with two thirds of the octahedral sites occupied by Fe^{3+} ions (Fig. 1). Natural hematite, which is a common compound in rocks and soils and a valuable iron ore, usually contains a certain quantity of metal cations other than iron [1,2]. Synthetic hematite can be prepared in different forms (particles of various size and shape, thin films, etc.) exhibiting properties suitable for a number of applications (pigment, catalyst, photocatalyst, photoanode, gas sensor, abrasive, etc.) [1,4–9]. Along with the size and shape of hematite crystallites and particles, doping with various metal cations is also an important factor that can improve particular properties (absorption, adsorption, catalytic, photocatalytic, electrical, thermal, etc.) of hematite which are needed for some of these applications [10–13]. Generally, the properties of hematite are altered by doping - in some cases only slightly, in others significantly, depending on the doped cation and the monitored property [1,2].

Doping of hematite with various metal (M) cations has been extensively reported in literature [1,2]. Generally, trivalent dopant cations replace Fe^{3+} ions in their octahedral sites (substitution) whereas divalent and tetravalent cations occupy both substitutional and interstitial octahedral sites [14–17]. In the case of some trivalent cations (Rh^{3+}, Cr^{3+}, Ga^{3+}) the solid solutions of hematite and isostructural metal oxide (M_2O_3) in the whole M to Fe ratio range (0:100 to 100:0) were reported [18–21]. The same charge, similar ionic radius and the existence of metal oxide with hematite (corundum) structure are necessary factors required for the formation of solid solutions in the broad M to Fe ratio range. All these factors are satisfied in the case of Rh^{3+}, Cr^{3+} and Ga^{3+} ions.

In the case of In^{3+} ion substitution for Fe^{3+} in hematite, the charge is the same and indium oxide (In_2O_3) with corundum structure exists [22,23], but the ionic radius is significantly larger (0.80 Å for In^{3+} compared with 0.645 Å for Fe^{3+} in octahedral coordination and a high-spin state) [24]. Only a partial substitution of In^{3+} for Fe^{3+} in α-Fe_2O_3 has been obtained in samples prepared by coprecipitation and calcination [25], by hydrothermal treatment [26] or by ball milling [27,28]. However, a solid solution α-$(Fe_{1-x}In_x)_2O_3$ in the whole In/Fe range was reported for samples prepared by solid-state reaction at high pressure and temperature [29].

* Corresponding author.
E-mail address: krehul@irb.hr (S. Krehula).

http://dx.doi.org/10.1016/j.jallcom.2016.11.022
0925-8388/

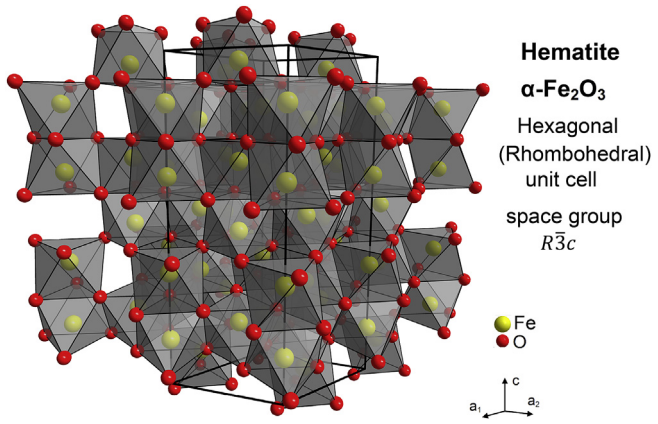

Fig. 1. Crystal structure of α-Fe_2O_3 represented by the cation polyhedra. The space group, crystallographic axes and unit cell are designated.

Indium doping in some other iron oxides has also been investigated. Replacement of magnetic Fe^{3+} ions by nonmagnetic In^{3+} ions in ε-Fe_2O_3 induced significant changes in magnetic and millimeter wave absorption properties [30–32]. In-doped n-Fe_2O_3 thin film electrodes showed higher photocurrent density [33,34]. ^{111}In-substituted Fe_3O_4 nanoparticles were prepared in order to obtain non-leachable radiolabelled Fe_3O_4 nanoparticles for application in magnetic resonance imaging [35].

In contrast to former studies, where In-doped hematite was prepared by a solid-state reaction of oxides [29], calcination of mixed hydroxides [25], hydrothermal treatment of mixed aqueous salt solutions [26] or ball-milling of oxides [27,28], in the present work In-doped hematite was prepared by calcination of In-doped goethite (α-FeOOH). In our previous work [36] In-doped goethite samples were synthesized by the coprecipitation method and their properties were investigated. A significant influence of In doping on the unit cell size, hyperfine magnetic field, crystallite and particle size, IR and UV–Vis spectra and thermal properties of goethite was observed. In the present work In-doped hematite samples were prepared by calcination of these In-doped goethite samples at 500 °C. Properties of thus obtained In-doped hematite samples were investigated using different instrumental techniques.

2. Experimental

2.1. Sample preparation

Hematite and In-doped (5, 10, 15 and 20 mol% In) hematite samples were prepared from goethite and In-doped goethite samples [36] by calcination at 500 °C for 2 h. The temperature in the furnace was raised to the corresponding value at a rate of 5 °C/min. The calcined samples were cooled down naturally to room temperature within the furnace. Obtained powder samples were characterized using X-ray powder diffraction (XRD), field emission scanning electron microscopy (FE-SEM), ^{57}Fe Mössbauer spectroscopy, diffuse reflectance UV–Vis–NIR spectroscopy and Fourier transform infrared (FT-IR) spectroscopy. Magnetic properties of selected samples were also analyzed.

2.2. Instrumentation

X-ray powder diffractometer APD 2000 (CuKα radiation, graphite monochromator, NaI–Tl detector) manufactured by *Ital-Structures* (*G.N.R. s.r.l.*, Novara, Italy) was used. Potassium bromide (*Sigma-Aldrich*, ≥99% trace metals basis) was used as an internal standard. The Rietveld refinements of XRD data were performed using the MAUD program [37].

^{57}Fe Mössbauer spectra were recorded at 20 °C (293 K) in the transmission mode using a standard *WissEl* (Starnberg, Germany) instrumental configuration. A ^{57}Co/Rh Mössbauer source was used. The velocity scale and all data refer to the metallic α-Fe absorber at 20 °C. A quantitative analysis of the recorded spectra was made using the *MossWinn* program [38].

Magnetic measurements were performed on selected samples in the Physical Properties Measurement System (PPMS) from Quantum Design with a Vibration Sample Magnetometer (VSM) insert as well as in a S700X SQUID susceptometer from *Cryogenics Ltd*.

A *JEOL* thermal field emission scanning electron microscope (FE-SEM, model JSM-7000F) was used for the observation of particle morphology. The FE-SEM was connected to the *Oxford Instruments* EDS/INCA 350 energy dispersive X-ray analyzer for elemental analysis. The specimens were not coated with an electrically conductive surface layer.

Fourier transform infrared (FT-IR) spectra were recorded at RT using a *Perkin Elmer Spectrum One* spectrometer. All powder samples for this purpose were ground using agate mortar and pestle, mixed with spectroscopically pure KBr and pressed into small disks.

Diffuse reflectance UV–Vis–NIR spectra were obtained at 20 °C using a *Shimadzu* UV–Vis–NIR spectrometer (model UV-3600) equipped with an integrated sphere. Barium sulfate was used as reference.

3. Results and discussion

3.1. X-ray powder diffraction

The X-ray powder diffraction patterns of synthesized samples (Fig. 2) revealed the presence of a hematite-like phase as almost a

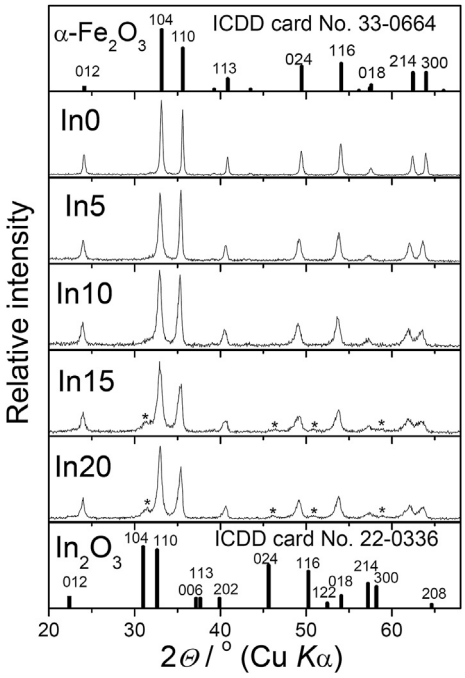

Fig. 2. XRD powder patterns of prepared In-doped hematite samples. Positions and intensities of diffraction lines of α-Fe_2O_3 and hexagonal In_2O_3 phases as given in the Powder Diffraction File (PDF) of the International Centre for Diffraction Data (ICDD) are also shown. Diffraction lines assigned by * in the patterns of samples In15 and In20 correspond to the In_2O_3 phase.

single phase in all five samples. The XRD pattern of sample In0 (containing no In) corresponds to pure hematite, α-Fe_2O_3 (ICDD card No. 33-0664). The hematite-like phase is present as a single phase in samples containing 5 mol% (sample In5) and 10 mol% (sample In10) of indium. A small amount of hexagonal In_2O_3 (ICDD card No. 22-0336), a phase isostructural to hematite, is also present in samples containing higher amounts of indium (samples In15 and In 20, diffraction lines assigned by asterisk).

A higher indium content in samples caused a shift of the α-Fe_2O_3 diffraction lines to lower 2Θ angles. This indicates the expansion of the α-Fe_2O_3 unit cell due to In substitution, which is in line with the larger radius of In^{3+} ions (r = 0.80 Å) compared with Fe^{3+} ions (r = 0.645 Å) in octahedral coordination and a high-spin state [24]. Unit cell parameters (Table 1) were determined by the Rietveld refinement of recorded XRD patterns using the MAUD program [37]. The dependence of the α-Fe_2O_3 unit cell volume on the In content is shown in Fig. 3 (the indium content in powder samples approximately equal to nominal values in initial solutions was confirmed by EDS). The unit cell volume increased significantly from 302.1 $Å^3$ in undoped α-Fe_2O_3 to 306.2 $Å^3$ in sample In5 and 308.7 $Å^3$ in sample In10 and remained approximately constant at a higher In content. From the curve in Fig. 3 the maximum In-for-Fe substitution in hematite can be estimated at about 8 mol%.

In-for-Fe substitution in In-doped hematite samples also caused a broadening of diffraction lines (Fig. 2, Table 1). Interestingly, this is unlike the precursor In-doped goethite samples where the diffraction lines are narrower with increased In-for-Fe substitution [36]. It is known from literature that the XRD patterns of hematite obtained by thermal transformation of goethite show a narrowing of diffraction lines with raised thermal treatment temperature due to decreased microstrain and enlarged crystallite size [39,40]. The incorporation of some metal cations (for example Al^{3+}, Cr^{3+}, Ga^{3+}) into the structure of iron oxides may induce their higher thermal stability [41–43] due to stronger M–O bonds compared with Fe–O bonds. In our previous work it was observed that the In-for-Fe substitution in goethite resulted in a higher goethite dehydroxylation temperature [36]. In the present work, broadening of diffraction lines by increased In-for-Fe substitution in hematite (Fig. 2, Table 1) can be explained by a lower effect of heating on the decrease in microstrain and enlargement in crystallite size in more doped hematite samples due to their higher thermal stability. Higher thermal stability of In-doped hematite is a consequence of stronger In–O bonds compared with Fe–O bonds. Broader diffraction lines with increased doping were also observed for Al- and Ga-doped hematite obtained by calcination of doped goethite at 500 °C [21,44]. Like the In dopant, Al and Ga dopants also induced higher goethite thermal stability.

3.2. ^{57}Fe Mössbauer spectroscopy

The ^{57}Fe Mössbauer spectra (recorded at 20 °C) of prepared hematite sample (In0) and In-doped hematite samples are shown in Fig. 4, left side. The calculated Mössbauer parameters and phase identification are given in Table 2. The magnetic sextet with

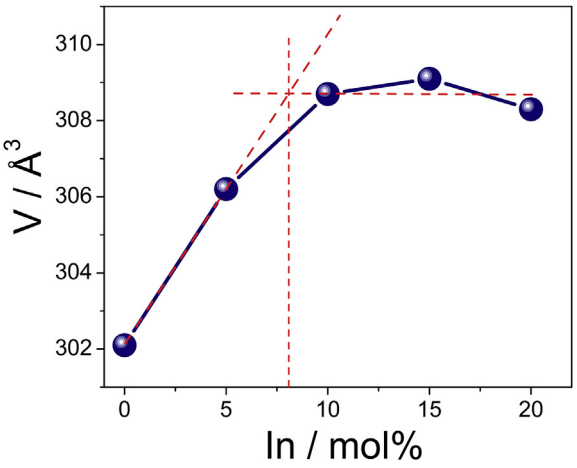

Fig. 3. Graphical representation of the dependence of unit cell volume on the In content in In-doped hematite samples, as determined using XRD.

Mössbauer parameters characteristic of hematite (Table 2) is almost a single component in these spectra. It was fitted using the distribution of the hyperfine magnetic field (HMF or B_{hf}) (Fig. 4, right side). The reduction of HMF and a deviation in quadrupole splitting (2ε) relative to the values of these Mössbauer parameters of standard well-crystalline hematite [45] are typical of imperfectly crystalline hematite prepared by thermal dehydroxylation of goethite [21,44,46–48]. A minor component (quadrupole doublet) is likely to originate from Fe^{3+} ions incorporated into the In_2O_3 phase. The replacement of magnetic Fe^{3+} ions by non-magnetic In^{3+} ions in hematite causes an interruption of the super-exchange interaction between Fe^{3+} ions via O^{2-} ions which results in the reduction of HMF on Fe atoms located in the vicinity of In atoms. This was expressed in Mössbauer spectra as increased line width of the hematite sextet (Fig. 4, left side) due to a broadening of HMF distribution toward lower values (Fig. 4, right side). Average HMF in hematite is significantly reduced by In doping, whereas the isomer shift and quadrupole splitting show no change (Table 2). The dependence of average HMF on the indium content in In-doped hematite samples is shown in Fig. 5.

3.3. Magnetic measurements

Magnetic properties of hematite have been broadly investigated using different techniques (magnetic measurement methods, neutron diffraction, Mössbauer spectroscopy, etc.) [2,49–59]. At and above room temperature (up to the Néel temperature of about 955 K) magnetic ordering in hematite is nearly antiferromagnetic in the hexagonal (001) (rhombohedral (111)) plane, but, due to the slight canting of magnetic moments from the antiferromagnetic axis, a small net magnetization is present (a weakly ferromagnetic state) [60,61]. At temperatures below about 260 K magnetic moments change their orientation to the direction along the hexagonal

Table 1
Unit cell parameters of In-doped hematite samples.

Sample	100·[In]/([In]+[Fe])	Unit cell parameter/Å		V/$Å^3$	FWHM/°2Θ	
		a	c		(104)	(110)
In0	0.0	5.0360 (3)	13.754 (1)	302.1 (1)	0.282	0.157
In5	5.0	5.0629 (6)	13.793 (2)	306.2 (1)	0.440	0.297
In10	10.0	5.0809 (5)	13.809 (2)	308.7 (1)	0.499	0.468
In15	15.0	5.0856 (3)	13.800 (3)	309.1 (1)	0.599	0.591
In20	20.0	5.0776 (8)	13.806 (2)	308.3 (2)	0.479	0.530

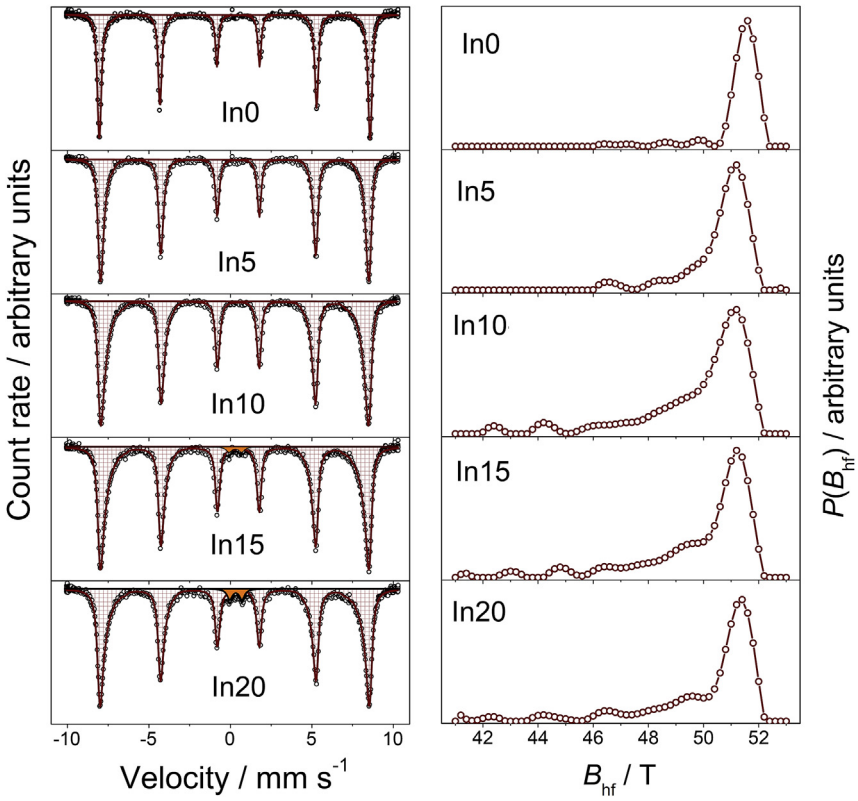

Fig. 4. ^{57}Fe Mössbauer spectra of In-doped hematite samples recorded at 20 °C (left side) and the distribution of hyperfine magnetic field in In-doped hematite samples, as calculated by fitting the recorded ^{57}Fe Mössbauer spectra (right side).

Table 2
^{57}Fe Mössbauer parameters (20 °C) calculated for the recorded In-doped hematite samples and phase identification.

Sample	Spectral component	δ (mm s^{-1})	2ε (mm s^{-1})	Δ (mm s^{-1})	$\langle B_{hf}\rangle$ (T)	Γ (mm s^{-1})	Area (%)	Phase
In0	Sextet	0.37	−0.22	–	51.5	0.23	100.0	α-Fe_2O_3
In5	Sextet	0.37	−0.22	–	50.6	0.27	100.0	α-$(Fe,In)_2O_3$
In10	Sextet	0.37	−0.22	–	49.9	0.28	100.0	α-$(Fe,In)_2O_3$
In15	Sextet	0.37	−0.22	–	49.8	0.29	98.3	α-$(Fe,In)_2O_3$
	Doublet	0.33	–	0.77	–	0.40	1.7	$(In,Fe)_2O_3$
In20	Sextet	0.37	−0.22	–	50.1	0.29	96.6	α-$(Fe,In)_2O_3$
	Doublet	0.33	–	0.75	–	0.38	3.4	$(In,Fe)_2O_3$

Errors: $\delta = \pm 0.01$ mm s^{-1}, $2\varepsilon = \pm 0.01$ mm s^{-1}, $\Delta = \pm 0.01$ mm s^{-1}, $B_{hf} = \pm 0.2$ T.
Isomer shift is given relative to α-Fe.

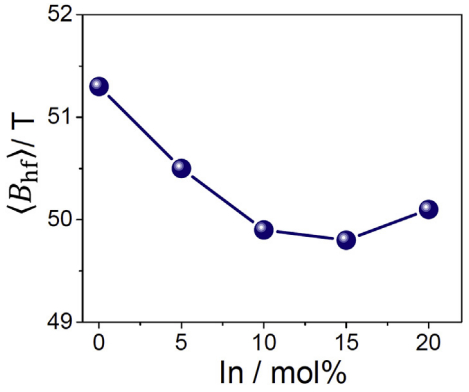

Fig. 5. Graphical representation of the dependence of an average hyperfine magnetic field on the In content in In-doped hematite samples.

c-axis [001] (rhombohedral [111] axis) with exactly antiparallel magnetic sublattices (an antiferromagnetic state). This magnetic phase transition in hematite at about 260 K is called the Morin transition after F.J. Morin who first observed it by measuring the temperature dependence of hematite magnetic susceptibility [49]. The Morin transition temperature or the Morin temperature (T_M) is dependent on the crystallinity of hematite sample as well as on the doping with metal cations. The lower crystallinity and doping with most metal cations affect the shift of T_M below 260 K [2,51,62–67]. Hematite of very low crystallinity or doped with significant amounts of metal cations shows no Morin transition down to the very low temperatures [21,62,68,69]. The shift of T_M to higher temperatures (above RT) was observed for hematite doped with some platinum group metal cations [18,48,70–75].

Temperature dependence of magnetization (normalized to the value at 100 K) for hematite sample (In0) and In-doped hematite samples (In5 and In10) is shown in Fig. 6. A significant increase in magnetization at temperatures from 200 to 250 K due to the Morin transition was observed for the undoped hematite sample In0. A difference of 14 K in the Morin transition temperature between ZFC and FC curves is visible (Inset Fig. 6). Thermal hysteresis at the Morin transition has been observed for different hematite samples

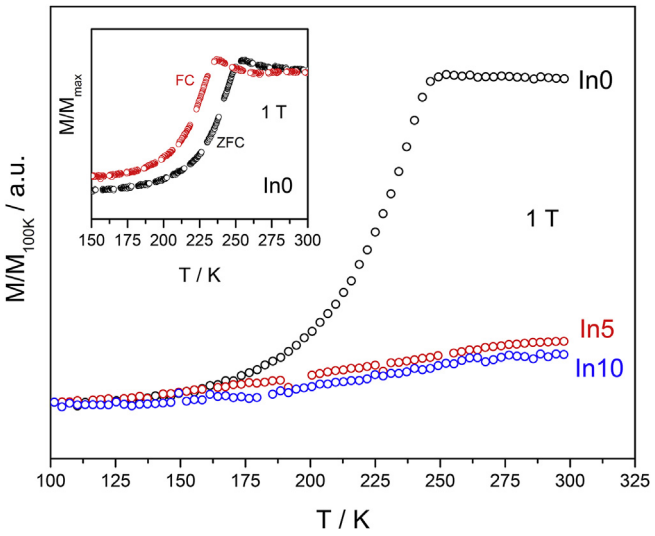

Fig. 6. Temperature dependence of magnetization normalized to the value at 100 K for hematite sample (In0) and In-doped hematite samples (In5 and In10). Inset: Zero-field-cooled (ZFC) and field-cooled (FC) curves for In0 around Morin transition.

[55,66] and its width is dependent on the size and crystallinity of hematite particles. The drop in T_M below 260 K in hematite sample In0 is caused by the lower crystallinity of hematite obtained by goethite dehydroxylation. The M-T curves of In-doped hematite samples In5 and In10 show no indication of the Morin transition. These results are in line with the neutron diffraction study of Sváb and Krén [63] who observed a disappearance of the Morin transition in hematite doped with 1.5 mol% of In.

3.4. FE-SEM

The particle size and morphology in In-doped hematite samples were observed by FE-SEM, with the characteristic images being shown in Figs. 7 and 8. Hematite and In-doped hematite particles retained the morphology of precursor goethite and In-doped goethite particles studied in the previous work [36]. Lath-shaped particles common for hematite formed by dehydroxylation of goethite are present in the undoped sample In0 (Fig. 7). Indium doping influenced a significant increase in the length and width of lath-shaped hematite particles (samples In5 and In10, Fig. 7). In-doped hematite particles also show a much better shape preservation compared with undoped hematite particles, due to higher thermal stability (Chapter 3.1). In the FE-SEM images of samples In15 and In20 (Fig. 8) even larger lath-shaped particles are visible. These particles are arranged in the worm-like agglomerates a few micrometers long (Fig. 8, bottom).

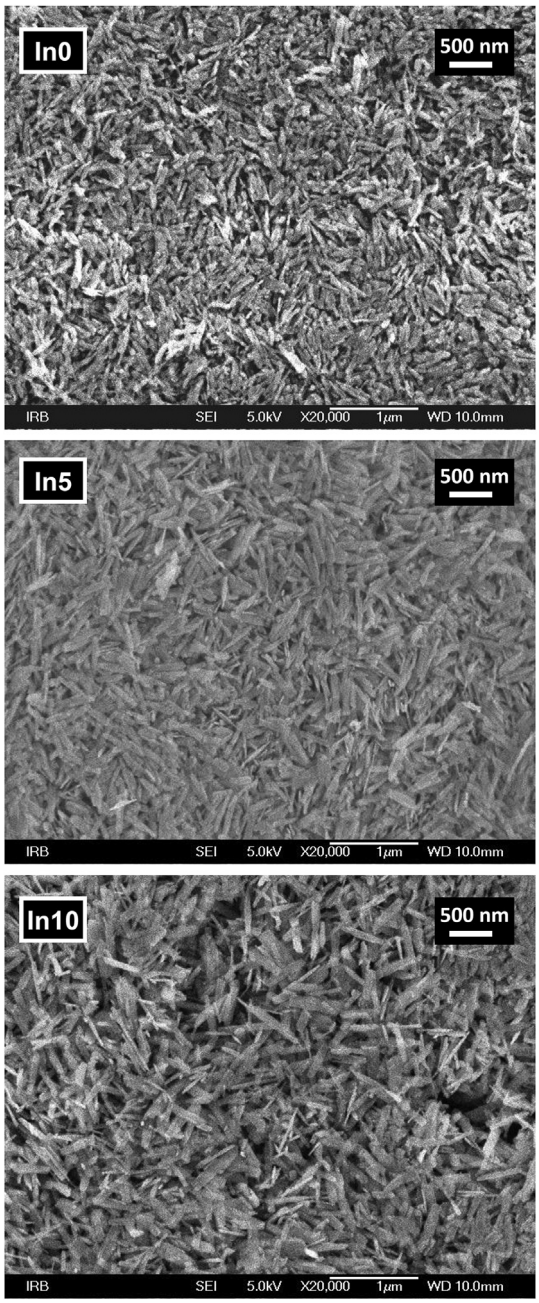

Fig. 7. FE-SEM images of hematite sample In0 and In-doped hematite samples In5 and In10.

3.5. FT-IR spectroscopy

A characteristic part of the FT-IR spectra (from 800 to 490 cm^{-1}) of the prepared In-doped hematite samples is shown in Fig. 9 and the positions of absorption bands are assigned. Generally, the positions of IR bands of hematite are dependent on particle shape [76–78]. The IR bands of hematite sample (In0) at 635 and 528 cm^{-1} are typical of lath-like hematite particles obtained by heating goethite particles of the same shape [76,79]. These bands correspond to A_{2u} (polarization parallel to the crystallographic *c*-axis) and E_u (polarization perpendicular to the crystallographic *c*-axis) normal modes of lattice vibration, respectively [76]. In the spectra of samples In5 and In10 the A_{2u} band was shifted slightly to higher wavenumbers and the E_u band to lower wavenumbers due to a changed shape of lath-like hematite particles (Fig. 7). Spectral band broadening at a higher indium content was most likely caused by lower crystallinity of In-doped hematite samples (chapter 3.1).

Band positions in IR spectra also depend on the mass of ions and bond strength. The shift of IR bands to higher wavenumbers was observed in the case of hematite doping with Al [80,81] and Ga [21] due to different mass of ions and bond strength. In doping in hematite did not produce a significant shift in the position of IR bands presumably because the effect of stronger In–O bonds and the effect of heavier In^{3+} ions cancel each other.

3.6. Diffuse reflectance UV–Vis–NIR spectroscopy

The diffuse reflectance UV–Vis–NIR spectra of hematite and In-

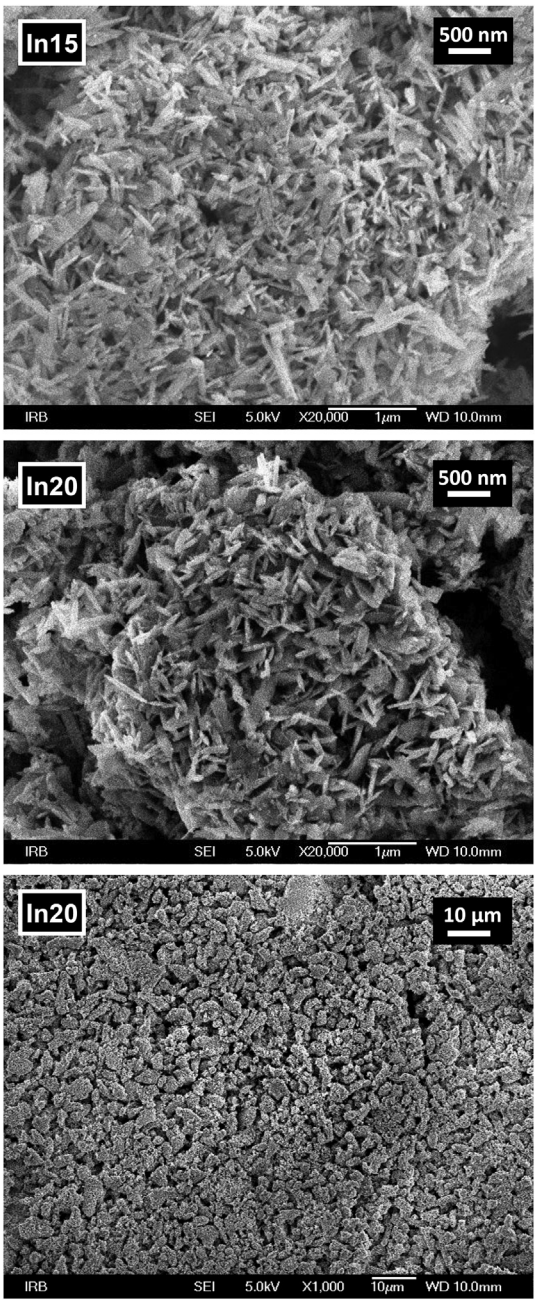

Fig. 8. FE-SEM images of In-doped hematite samples In15 and In20.

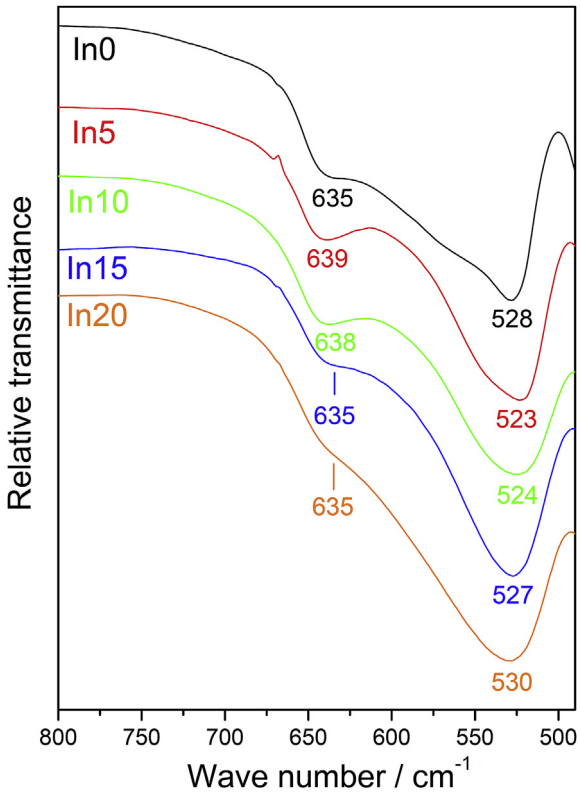

Fig. 9. FT-IR spectra of In-doped hematite samples.

doped hematite samples in the range from 200 to 1500 nm are shown in Fig. 10. The positions of absorption bands in these spectra are given in Table 3. The bands are assigned to corresponding electronic state transitions according to Sherman and Waite [82]. The spectrum of sample In0 (pure hematite) is similar to the hematite spectrum reported by Sherman and Waite [82]. In the NIR spectral region a weak and broad absorption band centered at about 880 nm is assigned to the $^6A_1 \rightarrow {}^4T_1(^4G)$ ligand field transition, which corresponds to electron excitation from the Fe^{3+} ground state $(t_{2g}^{\alpha})^3(e_g^{\alpha})^2$ to the first excited state $(t_{2g}^{\alpha})^3(t_{2g}^{\beta})^1(e_g^{\alpha})^1$. In the visible part of the spectrum the first feature is a shoulder at about 660 nm which is assigned to the $^6A_1 \rightarrow {}^4T_2(^4G)$ ligand field transition. A medium intensity band at about 520 nm corresponds to the electron pair transition $^6A_1 + {}^6A_1 \rightarrow {}^4T_1 + {}^4T_1$ (resulting from the magnetic coupling of adjacent Fe^{3+} cations). The most intense bands in the UV–Vis–NIR spectrum of hematite (as well as other iron oxides and oxyhydroxides) in the range between 270 and 500 nm have been assigned to the "spin-flip" ligand field transitions of Fe^{3+}, $e_g^{\alpha} \rightarrow e_g^{\beta}$ and $t_{2g}^{\alpha} \rightarrow t_{2g}^{\beta}$ (a change in the spin orientation of one electron in relation to the ground state configuration). The strongest band at about 395 nm corresponds to the $^6A_1 \rightarrow {}^4E(^4D)$ transition and the band at 315 nm to the $^6A_1 \rightarrow {}^4T_1(^4P)$ transition. A band at about 280 nm is assigned to the $6t_{1u} \rightarrow 2t_{2g}$ ligand-to-metal charge-transfer transition.

A higher In content in In-doped hematite samples led to a lower relative intensity of absorption bands in UV–Vis–NIR spectra due

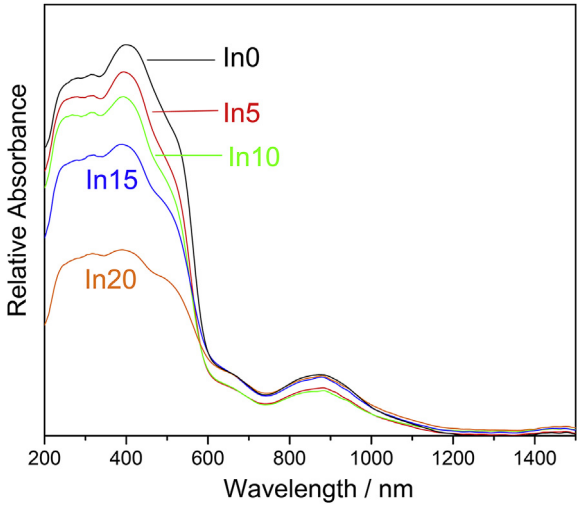

Fig. 10. UV–Vis–NIR spectra of In-doped hematite samples.

Table 3
Positions of absorption bands in the UV–Vis–NIR spectra of In-doped hematite samples. Bands are assigned to corresponding electronic state transitions according to Sherman and Waite [66].

Sample	Band position/nm					
	$6t_{1u} \rightarrow 2t_{2g}$ (LMCT)	$^6A_1 \rightarrow {}^4T_1$ (^4P)	$^6A_1 \rightarrow {}^4E$ (^4D)	$2(^6A_1) \rightarrow 2(^4T_1$ (^4G))	$^6A_1 \rightarrow {}^4T_2$ (^4G)	$^6A_1 \rightarrow {}^4T_1$ (^4G)
In0	~280	315	395	~520	~660	880
In5	~280	319	393	~520	~660	882
In10	~280	315	392	~520	~660	882
In15	~280	320	391	~520	~660	878
In20	~280	317	391	~520	~660	881

to a lower content of Fe^{3+} ions and a higher content of In^{3+} ions with no *d*-electron transitions (In^{3+} ions have completely filled 4d atomic orbital, electron configuration [Kr] $4d^{10}$). The strongest band at about 395 nm showed the largest intensity lowering by indium doping. No significant shift in the position of absorption bands with In doping was observed (Table 3).

4. Conclusions

Indium-doped hematite samples were synthesized by calcination of indium-doped goethite samples at 500 °C. The influence of indium doping on the properties of hematite was investigated using different instrumental techniques. Maximum In^{3+}-for-Fe^{3+} substitution in thus prepared hematite was estimated at about 8 mol%. Indium substitution in hematite caused:

- An increase in the unit cell size, in line with the larger radius of In^{3+} ions.
- A decrease in crystallite size due to higher thermal stability of In-doped hematite.
- A reduction of the hyperfine magnetic field caused by the dilution of the magnetic lattice by the replacement of magnetic Fe^{3+} ions with diamagnetic In^{3+} ions.
- A disappearance of the magnetic phase transition (Morin transition).
- An increase in the length and width of lath-shaped hematite particles with a better preserved shape.
- A shift in the position of IR absorption bands due to an increase in the length and width of lath-shaped hematite particles.
- A lower relative intensity of absorption bands in UV–Vis–NIR spectra due to a lower content of Fe^{3+} ions and a higher content of In^{3+} ions with no *d*-electron transitions.

Acknowledgment

The financial support by the Croatian Centre of Excellence for Advanced Materials and Sensing Devices is gratefully acknowledged.

References

[1] R.M. Cornell, U. Schwertmann, The Iron Oxides, Structure, Properties, Reactions, Occurrence and Uses, second ed., Wiley-VCH, Weinheim, 2003.
[2] A.H. Morrish, Canted Antiferromagnetism: Hematite, World Scientific, Singapore, 1994.
[3] R.L. Blake, R.E. Hessevick, T. Zoltai, L.W. Finger, Am. Mineral. 51 (1966) 123–129.
[4] J. Wang, W.B. White, J.H. Adair, J. Am. Ceram. Soc. 88 (2005) 3449–3454.
[5] B. Sun, J. Horvat, H.S. Kim, W.-S. Kim, J. Ahn, G. Wang, J. Phys. Chem. C 114 (2010) 18753–18761.
[6] K. Sivula, F. Le Formal, M. Grätzel, ChemSusChem 4 (2011) 432–449.
[7] J. Ma, J. Teo, L. Mei, Z. Zhong, Q. Li, T. Wang, X. Duan, J. Lian, W. Zheng, J. Mater. Chem. 22 (2012) 11694–11700.
[8] Y. Liu, C. Yu, W. Dai, X. Gao, H. Qian, Y. Hua, X. Hu, J. Alloys Compd. 551 (2013) 440–443.
[9] Z. Lu, S.-H. Lee, S.V. Babu, E. Matijević, J. Colloid Interface Sci. 261 (2003) 55–64.
[10] G.C. de Araújo, M. do Carmo Rangel, Catal. Today 62 (2000) 201–207.
[11] O.K. Tan, W. Cao, W. Zhu, J.W. Chai, J.S. Pan, Sens. Actuators B 93 (2003) 396–401.
[12] N.T. Hahn, C.B. Mullins, Chem. Mater. 22 (2010) 6474–6482.
[13] J. Frydrych, L. Machala, J. Tucek, K. Siskova, J. Filip, J. Pechousek, K. Safarova, M. Vondracek, J.H. Seo, O. Schneeweiss, M. Grätzel, K. Sivula, R. Zboril, J. Mater. Chem. 22 (2012) 23232–23239.
[14] F.J. Berry, C. Greaves, J. McManus, M. Mortimer, G. Oates, J. Solid State Chem. 130 (1997) 272–276.
[15] F.J. Berry, A. Bohorquez, C. Greaves, J. McManus, E.A. Moore, M. Mortimer, J. Solid State Chem. 140 (1998) 428–430.
[16] F.J. Berry, A. Bohorquez, E.A. Moore, Solid State Commun. 109 (1999) 207–211.
[17] F.J. Berry, C. Greaves, Ö. Helgason, J. McManus, H.M. Palmer, R.T. Williams, J. Solid State Chem. 151 (2000) 157–162.
[18] J.M.D. Coey, G.A. Sawatzky, J. Phys. C. Solid St. Phys. 4 (1971) 2386–2407.
[19] J.M.G. Amores, V.S. Escribano, G. Busca, E.F. Lopez, M. Saidi, J. Mater. Chem. 11 (2001) 3234–3240.
[20] T. Grygar, P. Bezdička, J. Dědeček, E. Petrovský, O. Schneeweiss, Ceram. Silikáty 47 (2003) 32–39.
[21] S. Krehula, M. Ristić, S. Kubuki, Y. Iida, M. Perović, M. Fabián, S. Musić, J. Alloys Comp. 634 (2015) 130–141.
[22] A.N. Christensen, R. Grønbæk, S.E. Rasmussen, Acta Chem. Scand. 18 (1964) 1261–1266.
[23] M. Epifani, P. Siciliano, A. Gurlo, N. Barsan, U. Weimer, J. Am. Chem. Soc. 126 (2004) 4078–4079.
[24] R.D. Shannon, Acta Cryst. A32 (1976) 751–767.
[25] M. Ristić, S. Popović, M. Tonković, S. Musić, J. Mater. Sci. 26 (1991) 4225–4233.
[26] M. Sorescu, L. Diamandescu, D. Tarabasanu-Mihaila, J. Phys. Chem. Solids 65 (2004) 1719–1725.
[27] M. Sorescu, T. Xu, L. Diamandescu, J. Mater. Sci. 46 (2011) 2350–2358.
[28] M. Sorescu, T. Xu, L. Diamandescu, D. Hileman, Hyperfine Interact. 199 (2011) 365–386.
[29] C.T. Prewitt, R.D. Shannon, D.B. Rogers, A.W. Sleight, Inorg. Chem. 8 (1969) 1985–1993.
[30] S. Sakurai, S. Kuroki, H. Tokoro, K. Hashimoto, S. Ohkoshi, Adv. Funct. Mater. 17 (2007) 2278–2282.
[31] K. Yamada, H. Tokoro, M. Yoshikiyo, T. Yorinaga, A. Namai, S. Ohkoshi, J. Appl. Phys. 111 (2012) 07B506.
[32] M. Yoshikiyo, A. Namai, M. Nakajima, K. Yamaguchi, T. Suemoto, S. Ohkoshi, J. Appl. Phys. 115 (2014) 172613.
[33] W.B. Ingler Jr., S.U.M. Khan, Proc. Electrochem. Soc. 6 (2004) 124–133.
[34] W.B. Ingler Jr., D. Sporar, X. Deng, ECS Trans. 3 (2006) 253–259.
[35] J. Zeng, B. Jia, R. Qiao, C. Wang, L. Jing, F. Wang, M. Gao, Chem. Commun. 50 (2014) 2170–2172.
[36] S. Krehula, M. Ristić, S. Kubuki, Y. Iida, L. Kratofil Krehula, S. Musić, J. Alloys Compd. 658 (2016) 41–48.
[37] L. Lutteroti, MAUD (Material Analysis Using Diffraction), General Diffraction/Reflectivity Analysis Program. http://www.ing.unitn.it/~maud/index.html.
[38] Z. Klencsár, E. Kuzmann, A. Vértes, J. Radioanal, Nucl. Chem. 201 (1996) 105–118.
[39] J.L. Rendon, J. Cornejo, P. De Arambarri, C.J. Serna, J. Colloid Interface Sci. 92 (1983) 508–516.
[40] S. Gialanella, F. Girardi, G. Ischia, I. Lonardelli, M. Mattarelli, M. Montagna, J. Therm. Anal. Calorim. 102 (2010) 867–873.
[41] H.D. Ruan, R.J. Gilkes, Clays Clay Min. 43 (1995) 196–211.
[42] M.A. Wells, R.W. Fitzpatrick, R.J. Gilkes, Clays Clay Min. 54 (2006) 176–194.
[43] S. Krehula, L. Kratofil Krehula, S. Musić, J. Alloys Compd. 581 (2013) 335–343.
[44] E. De Grave, L.H. Bowen, S.B. Weed, J. Magn. Magn. Mater. 27 (1982) 98–108.
[45] E. Murad, J.H. Johnston, Iron oxides and oxyhydroxides, in: G.J. Long (Ed.), Mössbauer Spectroscopy Applied to Inorganic Chemistry, vol. 2, Plenum Publishing Corporation, New York, 1987, pp. 507–582.
[46] R.E. Vandenberghe, A.E. Verbeeck, E. De Grave, W. Stiers, Hyperfine Interact. 29 (1986) 1157–1160.
[47] E.E. Sileo, D.P. Daroca, C.A. Barrero, A.L. Larralde, M.S. Giberti, C. Saragovi, Chem. Geol. 238 (2007) 84–93.
[48] S. Krehula, G. Štefanić, K. Zadro, L. Kratofil Krehula, S. Musić, J. Alloys Compd. 545 (2012) 200–209.
[49] F.J. Morin, Phys. Rev. 78 (1950) 819–820.

[50] G.G. Shull, W.A. Strauser, E.O. Wollen, Phys. Rev. 83 (1951) 333–345.
[51] P.J. Besser, A.H. Morrish, C.V. Searle, Phys. Rev. 153 (1967) 632–640.
[52] D. Schroeer, R.C. Niniger, Phys. Rev. Lett. 19 (1967) 632–634.
[53] R.C. Niniger, D. Schroeer, Phys. Chem. Solids 39 (1978) 137–144.
[54] F. Bødker, M.F. Hansen, C.B. Koch, K. Lefmann, S. Mørup, Phys. Rev. B 61 (2000) 6826–6838.
[55] G.F. Goya, M. Veith, R. Rapalavicuite, H. Shen, S. Mathur, Appl. Phys. A 80 (2005) 1523–1526.
[56] Ö. Özdemir, D.J. Dunlop, J. Geophys. Res. 111 (2006) B12S03.
[57] M. Tadić, N. Čitaković, M. Panjan, Z. Stojanović, D. Marković, V. Spasojević, J. Alloys Compd. 509 (2011) 7639–7644.
[58] M. Tadić, N. Čitaković, M. Panjan, B. Stanojević, D. Marković, Đ. Jovanović, V. Spasojević, J. Alloys Compd. 543 (2012) 118–124.
[59] Ö. Özdemir, D.J. Dunlop, J. Geophys. Res. Solid Earth 119 (2014) 2582–2594.
[60] I. Dzyaloshinsky, J. Phys. Chem. Solids 4 (1958) 241–255.
[61] T. Moriya, Phys. Rev. 120 (1960) 91–98.
[62] E. Krén, B. Molnár, E. Sváb, É. Zsoldos, Solid State Commun. 15 (1974) 1707–1710.
[63] E. Sváb, E. Krén, J. Magn. Magn. Mater. 14 (1979) 184–186.
[64] R.E. Vandenberghe, E. Van San, E. De Grave, G.M. da Costa, Czech. J. Phys. 51 (2001) 663–675.
[65] R.D. Zysler, D. Fiorani, A.M. Testa, L. Suber, E. Agostinelli, M. Godinho, Phys. Rev. B 68 (2003) 212408.
[66] Ö. Özdemir, D.J. Dunlop, T.S. Berquó, Geochem. Geophys. Geosyst. 9 (2008) Q10Z01.
[67] Q. Liu, V. Barrón, J. Torrent, H. Qin, Y. Yu, Phys. Earth Planet. Inter. 183 (2010) 387–397.
[68] I. Ayub, F.J. Berry, R.L. Bilsborrow, Ö. Helgason, R.C. Mercader, E.A. Moore, S.J. Stewart, P.G. Wynn, J. Solid State Chem. 156 (2001) 408–414.
[69] M.-Z. Dang, D.G. Rancourt, J.E. Dutrizac, G. Lamarche, R. Provencher, Hyperfine Interact. 117 (1998) 271–319.
[70] J.Z. Liu, C.L. Fan, Phys. Lett. 105A (1984) 80–82.
[71] J.Z. Liu, J. Magn, Magn. Mater. 54–57 (1986) 901–902.
[72] Ö. Helgason, I. Ayub, F.J. Berry, E. Crabb, Hyperfine Interact. 141/142 (2002) 291–295.
[73] Ö. Helgason, J.-M. Greneche, F.J. Berry, F. Mosselmans, J. Phys. Condens. Matter 15 (2003) 2907–2915.
[74] N. Shimomura, S.P. Pati, Y. Sato, T. Nozaki, T. Shibata, K. Mibu, M. Sahashi, J. Appl. Phys. 117 (2015) 17C736.
[75] T. Mitsui, K. Mibu, M. Seto, M. Kurokuzu, S.P. Pati, T. Nozaki, M. Sahashi, J. Phys. Soc. Jpn. 85 (2016) 063601.
[76] C.J. Serna, J.L. Rendon, J.E. Iglesias, Spectrochim. Acta 38A (1982) 797–802.
[77] Y. Wang, A. Muramatsu, T. Sugimoto, Colloid Surf. A Phys. Eng. Asp. 134 (1998) 281–297.
[78] L. Chen, X. Yang, J. Chen, J. Liu, H. Wu, H. Zhan, C. Liang, M. Wu, Inorg. Chem. 49 (2010) 8411–8420.
[79] J.L. Rendon, C.J. Serna, Clay Min. 16 (1981) 375–381.
[80] S.A. Fysh, P.M. Fredericks, Clays Clay Min. 31 (1983) 377–382.
[81] V. Barron, J.L. Rendon, J. Torrent, C.J. Serna, Clays Clay Min. 32 (1984) 475–479.
[82] D.M. Sherman, T.D. Waite, Am. Min. 70 (1985) 1262–1269.